RSC Advances

RSC Advances

www.rsc.org/advances

ROYAL SOCIETY OF CHEMISTRY

www.rsc.org/advances

ARTICLE TYPE

Enhanced photoelectrochemical performance of the hierarchical micro/nano-structure TiO₂ mesoporous spheres with oxygen vacancies via hydrogenation

Xiaoying Zhang and Zhuoyuan Chen*

5

Abstract

The hierarchical micro/nano-structure TiO_2 mesoporous spheres with oxygen vacancies have been fabricated via a template-free strategy followed by hydrogenation and their photocatalytic performance has been explored. The hierarchical micro/nano-structure mesoporous spheres can act as a model

10 architecture for efficient photoelectrochemical devices because they can simultaneously offer abundant catalytic active sites, excellent light-scattering characteristics and a highly conductive pathway for charge carrier collection. More importantly, oxygen vacancies are introduced onto the surface of TiO_2 and function as shallow donors. The presence of oxygen vacancies not only boosts the light absorption but also improves the electrical conductivities of TiO_2, thus enhancing the optical response and electron-hole

15 separation. As a result, hierarchical micro/nano-structure TiO_2 mesoporous spheres with oxygen vacancies exhibit a remarkably enhanced photoelectrochemical performance.

Introduction

Since the breakthrough work by Fujishima and Honda in 1972,
20 TiO_2 has been undoubtedly regarded as one of the most excellent photocatalysts for a variety of solar-driven clean energy and environmental technologies.[1] However, pristine TiO_2 suffers from ineffective utilization of visible light due to its large band gap and low quantum yield because of the rapid recombination of
25 photogenerated carriers.

Recently, oxygen vacancies (Ov) in oxide semiconductors have been proposed as an alternative strategy to overcome the limitations mentioned above.[2-4] Lin et al. calculated the electronic band structures of nitrogen-doped and oxygen-deficient anatase
30 TiO_2 based on a density functional theory (DFT).[5] They found that the nitrogen doping mainly accounted for the absorption in the region of 400-500 nm, while the absorption occurring above 500 nm was primarily caused by the Ov. Subsequently, experimental progress has been achieved by Zhang and co-
35 workers.[6] They explored a novel plasma electrolysis method to synthesize high-quality TiO_2 with Ov, which exhibited strong optical absorption covering the range from ultraviolet to infrared. Furthermore, it was investigated that the blue-shift in the absorption edge and a notable increase in the long-wavelength
40 absorption was proportional to the concentration of Ov.[7] Therefore, it was believed that the Ov was responsible for the improvement of the visible light absorption of TiO_2, because Ov could introduce extra energy levels at approximately 0.75-1.18 eV below the conduction band (CB) of TiO_2.[8,9] Besides the
45 contribution of the enhanced visible light response, Ov were

demonstrated to serve as shallow donors (charge carriers) and account for the enhanced carrier density in hydrogenated TiO_2.[10-15] The increased carrier density played a critical role in the conductivity improvement and the recombination inhibition.
50 Therefore, Ov in TiO_2, especially induced by hydrogenation, could open up new opportunities for efficient photocatalysts.

In general, the TiO_2-photocatalyzed reduction and oxidation take place simultaneously at the surface of TiO_2. Consequently, the homogeneous TiO_2 photocatalysts are usually utilized as
55 nanoparticles to acquire high photocatalytic sites. However, a bothersome obstacle exists in those nanoparticles, where abundant grain boundaries and defects can hinder the achievement of high electrical conductivity.[16] For instance, the electron mobility in a nanoparticles film is about 0.01 $cm^2 V^{-1} S^{-1}$,
60 which is 2 orders of magnitude lower than that of a bulk single crystal (1 $cm^2 V^{-1} S^{-1}$).[17,18] As known, the recombination is the competition of the separation of photogenerated carriers. The low electron mobility negatively impacts charge separation process, thus resulting in a fast recombination of the photogenerated
65 carriers. Moreover, the excessive aggregation of nanopartices leads to substantial reduction of active surface areas, and thus depresses the catalytic activity. Additionally, their photon absorption is often limited by light reflection at the surface of a nanoparticles film.[19,20] One-dimensional nanostructured TiO_2,
70 such as nanotubes and nanowires, has been proposed because of the enhancements in charge transport, charge separation and light absorption[21,22]. However, the nanotubes or nanowires, compared to nanoparticles, have smaller surface areas, which can negatively affect charge transfer process. More current evidences have

demonstrated that the optical absorption of TiO_2 film can be promoted by additionally admixing larger TiO_2 particles in an optimal volume ratio.[23,24] Nevertheless, the drawback is that the introduction of larger particles will unavoidably reduce the
5 internal surface areas. Moreover, counteracting the enhancement effect of light scattering on the optical absorption, the incorporation of larger particles may lead to an undesirable increase in the electron diffusion length and, consequently, increase the recombination rate of photogenerated carriers.[25] To
10 address these issues mentioned above, the hierarchical micro/nano-structured design with mesopores may be an alternative, as suggested by Rolison, underlying "the Importance of Nothing and the Unimportance of Periodicity" in catalytic nanoarchitectures, where "nothing" is the porosity at the
15 nanoscale.[26] Such multilevel architectures, combining the advantages of nanoscale and microscale particles, enable materials a wealth of optimized properties.[27-29] For instance, this hierarchical structure can simultaneously provide abundant catalytic active sites, electronic conducting framework and mass
20 transport accessible porosity. In addition, the nanoarchitectures would be an ideal system to promote light scattering, and to enhance photon absorption for the increased electron-hole generation. Therefore, it is reasonably expected that the hierarchical micro/nano-structure TiO_2 mesoporous sphere with
25 Ov can be interesting candidates for further enhancing the photocatalytic performance.

Herein, the hierarchical micro/nano-structure TiO_2 mesoporous spheres with Ov were fabricated, consisting of primary nanoparticles and secondary colloidal spheres. The relationship
30 between morphology, surface structure and the photoelectrochemical performances was also explored by comparing with particulate TiO_2 samples with and without Ov.

Experimental Procedure

The hierarchical micro/nano-structure TiO_2 mesoporous spheres
35 with Ov were prepared via a template-free strategy followed by hydrogen-treatment. The hierarchical micro/nano-TiO_2 spheres (denoted as M-TiO_2) were firstly synthesized as described in our previous work without any variation.[30] In brief, 2 mL tetrabutoxytitanium was added to 50 mL ethylene glycol,
40 magnetically stirring for 8 hours at room temperature. The mixture was then poured into a solution containing 170 mL acetone and 2.7 mL water, stirring vigorously. And then the white precipitate was obtained by centrifugation, followed by washing with ethanol for five times and was dried at 50 °C. After
45 refluxing and centrifugation, the M-TiO_2 sample was obtained. For comparison, particulate TiO_2 (denoted as P-TiO_2) was also prepared by a sol-gel technique, according to a previous work.[31] Prior to hydrogenation, the synthesized TiO_2 was calcined in air at 500 °C for 2 h in order to improve the crystallization. The
50 hydrogenation was performed as follows: The as-prepared M-TiO_2 or P-TiO_2 samples were transferred to a quartz boat located at the center of a quartz tube, which was horizontally placed in a tubular furnace. Before starting the heat treatment, the inner tube of the furnace was evacuated and then purged with nitrogen, and
55 these two steps were repeated for four times. Subsequently, the inner tube of the furnace was evacuated and then purged with hydrogen, and these were repeated twice. Finally, the powders

were annealed at 350 °C for 1 h with 5 °C min^{-1} under 20 bar H_2. After being cooled to room temperature, the hydrogenated M-
60 TiO_2 or P-TiO_2 (denoted as HM-TiO_2 or HP-TiO_2) was obtained. The morphologies and the microstructures of the synthetic products were collected from field emission scanning electron microscopy (FESEM, HITACHI S-4800) and a high-resolution transmission electron microscope (HRTEM, FEI Tecnai G20, FEI
65 Company, USA). Their crystalline structures and bonding information were analyzed using X-ray diffraction (XRD, D/MAX-2500/PC; Rigaku Co., Tokyo, Japan) and X-ray photoelectron spectroscopy (XPS, Axis Ultra, Kratos Analytical Ltd., England). The optical absorption properties were recorded
70 in the wavelength range of 200-800 nm by using a Hitachi U4100 spectrophotometer that was equipped with an integrating sphere. N_2 adsorption-desorption measurements were carried out at 77 K using a Quantachrome Autosorb gas-sorption system.

The photocatalytic degradation measurements were performed
75 under illumination with a 300 W Xenon lamp (PLS-SXE300, Beijing Changtuo Co. Ltd., Beijing, China). 0.1 g prepared samples were mixed with an aqueous Rhodamine B (RhB) solution (100mL, 10 mg·L^{-1}) and was stirred vigorously in the dark for 30 min to achieve an adsorption-desorption equilibrium.
80 This mixture was then placed under a 300 W Xenon lamp and 3 mL suspension was withdrawn at regular intervals and stored in the dark. After the completion of the test, these suspensions were centrifuged at 10,000 rpm for 10 min to remove suspended particles, and the concentration of RhB was determined.
85 The prepared powder samples were fabricated into photoelectrodes as follows: 0.01 g of the obtained powder was added to 0.1 mL of deionized water in an agate mortar, and then carefully ground for 10 min, resulting in a homogeneous paste. This paste was evenly overlaid onto the conductive side of the
90 pre-cleaned fluorine-doped tin oxide glass substrate, followed by heat drying at 120°C for 2 h under vacuum condition. A copper wire was then connected to the conductive side of the fluorine-doped tin oxide glass using conductive silver tape. The substrate edges and the metal contact region were sealed with insulating
95 epoxy resin after the conductive silver tape had dried. The working electrode area is 0.8 cm^2.

The photoelectrochemical and electrochemical measurements were performed by an Electrochemical Workstation (CHI660D, Shanghai Chenhua Instrument Co., Ltd., Shanghai, China) in a
100 three-electrode cell with the obtained photoelectrode work electrode, Pt foil counter electrode and Ag/Ag$^+$ reference electrode. A 300 W Xenon lamp (PLS-SXE300, Beijing Changtuo Co. Ltd., Beijing, China) was used as the light source. The electrolyte used was 0.5 M Na_2SO_4 solution (pH=7). *J-V*
105 curves were collected with chopping every 4 s at a scan rate of 10 mV s^{-1} and the potential is from -1.0 V to +1.0 V *vs* Ag/AgCl. The variations of the photoinduced current density with time (i-t curve) were measured at a 0 V *vs* Ag/AgCl during a 3-cycle light switching on and off. The electrochemical impedance
110 spectroscopy (EIS) experiments were conducted under light illumination. The frequency range was chosen from 100 kHz to 100 mHz with an AC modulation signal of 5 mV at a dc potential of 0 V *vs* Ag/AgCl. The EIS results were analyzed using Zsimpwin software. Mott-Schottky plots were measured at 1000
115 Hz in the dark with the potential range between -0.8 V and 0.2 V

vs Ag/AgCl.

Results and Discussion
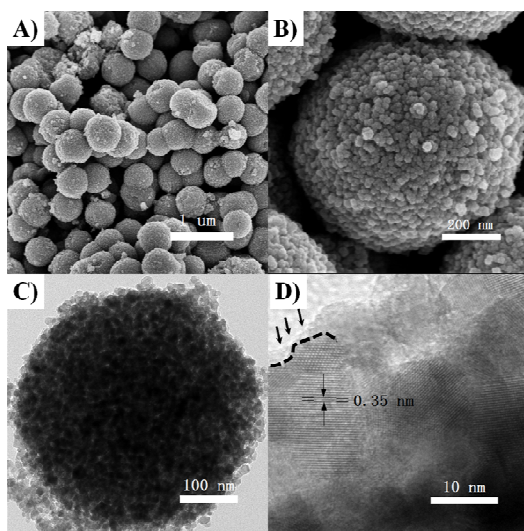
Fig. 1 (A) Low-magnification SEM image, (B) high-magnification SEM
image, (C) TEM and (D) HRTEM images of the as-prepared HM-TiO₂. In
(D), a short dashed curve is applied to outline a portion of the interface
between the crystalline core and the disordered outer layer (marked by
black arrows) of HM-TiO₂.

The microscopic morphology and crystal structure of the as-
prepared HM-TiO$_2$ were characterized by SEM, TEM and
HRTEM as shown in Fig. 1. Typical SEM image (Fig. 1a) at low
magnification reveals that the HM-TiO$_2$ samples consist of large
numbers of submicroscale spherical particles with a diameter of
500-550 nm. From the high magnification SEM image (Fig. 1b)
and the representative TEM image (Fig. 1c) of an individual
hierarchical sphere, these spherical particles are clearly observed
be constructed by hundreds of densely packed primary
nanoparticles with an average diameter of approximately 15 nm.
Further observation (Fig. 1d) indicates that a hydrogen-stabilized
amorphous layer is coated on the crystalline core after hydrogen
treatment, which is in a good agreement with the results shown in
literature.[32,33] In addition, well-defined lattice fringes with a d-
spacing of 0.35 nm can be well indexed to the (101) crystal plane
of anatase TiO$_2$ (Fig. 1d), which confirms that the core of as-
prepared HM-TiO$_2$ is highly crystallized. For comparison, Fig. S1
(ESI†) presents typical morphologies of the obtained HP-TiO$_2$,
from which numerous nanoparticles with an average diameter of
approximately 15 nm are randomly agglomerated, forming a
network of much larger clusters and thus reducing their specific
surface areas.
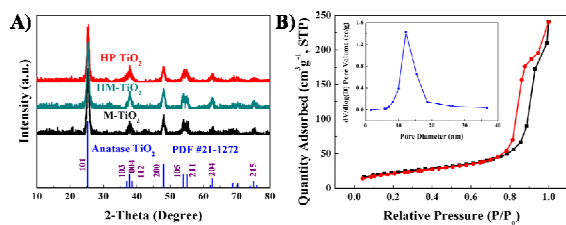
Fig. 2 (A) XRD patterns of the as-synthesized M-TiO₂, HP-TiO₂ and HM-

TiO$_2$. The XRD pattern of anatase TiO$_2$ is added as a reference. (B)
Nitrogen adsorption−desorption isotherm curve of the HM-TiO₂ sample
and its pore-size distribution (inset) obtained from desorption branch of
the isotherm using the BJH method.

The structural information of the as-synthesized HM-TiO$_2$ was
further analyzed by employing XRD and Nitrogen
adsorption−desorption isotherm and the relevant results are
shown in Fig. 2. XRD patterns collected from the resultant HP-
TiO$_2$ and HM-TiO$_2$ powders (Fig. 2A) illustrate that their
diffraction peaks can all be satisfactorily indexed to the anatase
phase TiO$_2$ (JCPDS No.21–1272). Such high anatase crystallinity
in the mesoporous TiO$_2$ is highly desirable in photocatalysis.
More importantly, no obvious broadening of the diffraction peaks
is observed between HP-TiO$_2$ and HM-TiO$_2$ samples, indicating
that there was no appreciable difference in nano-crystallite size
for the samples regardless of the various morphologies observed
by SEM. The average size of the primary nanocrystallite is
around 15 nm in diameter based on the Scherrer's formula, which
is consistent with the microscopic characterizations. Furthermore,
to detect the possible phase change taken place upon
hydrogenation, XRD pattern of M-TiO$_2$ was also collected. XRD
profiles for these two cases are almost identical, indicating that
the bulk lattice structure of anatase TiO$_2$ was well-preserved
during the hydrogenation procedure, which has also been
observed in the previous studies of hydrogenated TiO$_2$.[4]

Although no obvious pores were observed from TEM images
because of the overlapping of primary nanoparticles, the porous
structure of the product was clearly confirmed by nitrogen
adsorption−desorption isotherm and Barrett−Joyner−Halenda
(BJH) pore-size distribution analysis. As shown in Fig. 2B, the
recorded adsorption and desorption isotherm exhibits a
significant hysteresis and can be identified as Type *IV*, indicating
the presence of mesopores.[34] Furthermore, the BJH pore-size
distribution analysis shows that the as-synthesized HM-TiO$_2$
possesses a rather broad pore-size distribution with an average
pore radius of 13 nm. Overall, the aforementioned results
strongly demonstrate that the as-synthesized HM-TiO$_2$ possesses
a hierarchical architecture with plenty of different mesopores.
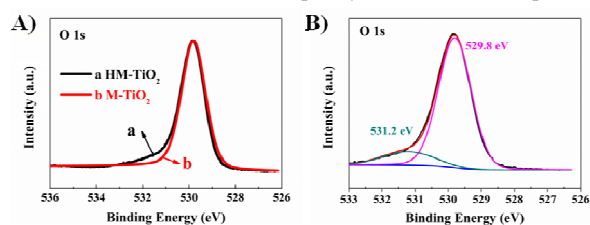
Fig. 3 (A) Overlay of normalized O1s XPS spectra of M-TiO₂ (curve a) and
HM-TiO₂ (curve b) ; (B) Normalized O 1s core level XPS spectra of HM-
TiO₂.

It is well known that hydrogenation could introduce additional
Ov into TiO$_2$, which serve as shallow donors and should be able
to improve the light response and the electrical conductivity of
TiO$_2$. To prove the presence of Ov, XPS was employed to
examine and compare the chemical composition and surface
oxidation states of M-TiO$_2$ and HM-TiO$_2$ samples. As shown in
Fig. S2A (ESI†), XPS survey spectra collected from M-TiO$_2$ and
HM-TiO$_2$ are essentially identical. Besides Ti and O, only a small
amount of C is observed in both samples. These results suggest

that no other impurities were introduced into TiO₂ mesoporous spheres through hydrogenation. From the O1s XPS spectra of the M-TiO₂ and HM-TiO₂ (Fig. 3A), HM-TiO₂ possesses a slightly broader peak with an additional shoulder at the higher binding energy by comparing with M-TiO₂. This broad peak could be deconvoluted into two peaks centered at 529.8 eV and 531.2 eV (Fig. 3B). While the peak centered at 529.8 eV is typically assigned to Ti−O bonds, the additional peak centered at 531.2 eV could be attributed to the adsorbed oxygen caused by Ov, indicating an increased density of Ov on the surface of HM-TiO₂.[35] This supported the observation of surface defects in the HRTEM image. After hydrogenation, Ti^{3+} is expected to form on the surface of TiO₂. However, there is no obvious difference in the high-resolution Ti2p spectra of M-TiO₂ and HM-TiO₂ samples (Fig. S2B, ESI†). Their Ti2p3/2 and Ti2p1/2 peaks are centered at the binding energies of 458.6 eV and 464.3 eV, which is consistent with the characteristic of Ti^{4+} in TiO₂.[36] It is not surprised that no Ti^{3+} is present at the particle surface because of its instability in air.[36]
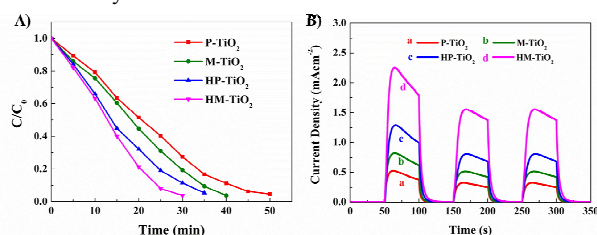
Fig. 4 Photoelectrochemical properties of the prepared P-TiO₂, M-TiO₂, HP-TiO₂ and HM-TiO₂. A) Photocatalytic activities for degradation of RhB under simulated solar illumination. C and C₀ are the RhB concentration after photocatalytic degradation and the equilibrium adsorption, respectively. B) Time-dependent profiles of photocurrent responses (i-t curves) collected at a constant bias of 0 V (*vs* Ag/AgCl) in 0.5 M NaSO₄ solution with light switched on and off.

To evaluate the effect of Ov and nanoarchitectures on the photoelectrochemical performance, various measurements were conducted and the results were shown in Fig. 4. Photocatalytic activity of the as-synthesized HM-TiO₂ was assessed by monitoring the degradation efficiency of RhB. For comparison, the photocatalytic behaviors of HP-TiO₂, M-TiO₂ and P-TiO₂ photocatalysts have also been investigated. Fig. 4A plots the relative changes in the concentration of RhB aqueous solution as a function of the reaction time. It can be clearly seen that the HM-TiO₂ and HP-TiO₂ samples take substantially shorter time for the dye degradation compared to the M-TiO₂ and P-TiO₂ samples. This difference may originate from the presence of Ov. Furthermore, these two hierarchical micro/nano-structured TiO₂ samples (HM-TiO₂ and M-TiO₂) exhibit higher photocatalytic activity than those of the particulate TiO₂ (HP-TiO₂ and P-TiO₂). More specifically, the HM-TiO₂ exhibits the highest photocatalytic activity, which can completely degrade RhB dye in 30 min under illumination. In contrast, the particulate HP-TiO₂ decomposes RhB dye in 35 min. Therefore, these results clearly indicate that the photocatalytic properties of TiO₂ can be significantly improved by introducing Ov and the hierarchical micro/nano-architecture.

Fig. 4B illustrates the photoelectric conversion performances of the as-prepared P-TiO₂, M-TiO₂, HP-TiO₂ and HM-TiO₂ samples,

based on the time-dependent profiles of photocurrent responses (i-t curves). The i-t curves also exhibit the enhanced photoelectrochemical property of HM-TiO₂. It is found that the rise and drop of the photocurrent collected from these TiO₂ samples all correspond well to each turn-on and –off event. The short-circuit photocurrent density of HM-TiO₂ is more than 1.5 mA cm⁻², whereas that of P-TiO₂ is less than 0.5 mAcm⁻². Such a comparison of the evolution of photocurrent density for these TiO₂ samples makes clear that the presence of hierarchical structure and Ov can boost the photoelectrochemical performances of as-prepared TiO₂ samples.
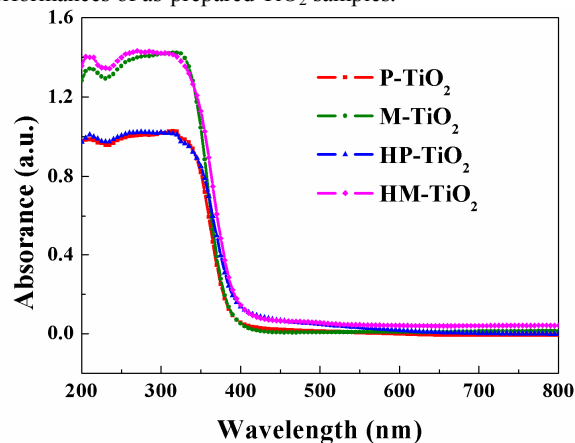
Fig. 5 UV/Vis diffuse reflectance spectra of the prepared P-TiO₂, M-TiO₂, HP-TiO₂ and HM-TiO₂.

In order to clarify the possible reasons for the enhanced photoelectrochemical performances of HM-TiO₂, its optical properties and electronic properties have been further studied. In Fig. 5, the optical properties of the as-synthesized TiO₂ samples were explored by UV/Vis diffuse reflectance spectra. In comparison with untreated M-TiO₂ and P-TiO₂ samples, a significant increase in the visible light absorption occurs for the HP-TiO₂ and HM-TiO₂, as indicated by the rising tail of the absorption curve in the long-wavelength range. After hydrogenation, an additional energy level of Ov, which is in the range of 0.75-1.18 eV lower than the CB of TiO₂, is introduced into TiO₂.[8] The strong UV absorption can be attributed to the electronic transition from the valence band to the CB. While the visible light absorption is due to the transitions from the TiO₂ valence band to the Ov levels or from the Ov to the TiO₂ conduction band.[11] The enhanced visible light absorption capability makes the HP-TiO₂ and HM-TiO₂ be effective photocatalysts for solar-driven applications by comparing with P-TiO₂ and M-TiO₂. Obviously, compared with HP-TiO₂, the obtained HM-TiO₂ has a significant optical absorption intensity increase in UV light region, but has no evident change in absorption band edges. This additional absorption could be predominantly attributed to light scattering, resulting from the presence of larger secondary spheres, which is in accordance to previous reports.[36,37] Typically, light scattering occurs with particles > 100 nm in diameter. Thus, the light scattering ability of the secondary spheres with 500-550 nm in diameter could be a plus to enhance the photon absorption and thus increases the amount of photogenerated electrons and holes available to participate in the photocatalytic process. These results are in line

with the photoelectrochemical properties obtained in Fig. 4.
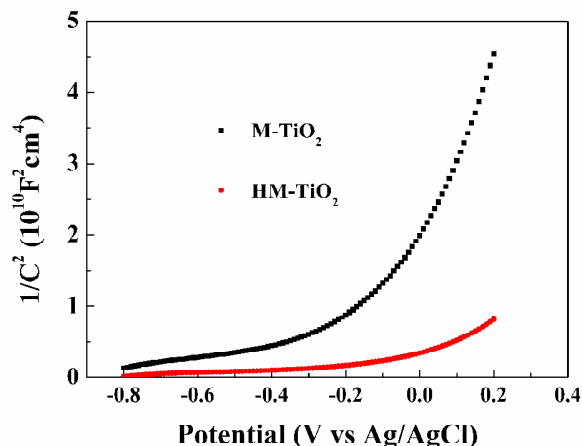
Fig. 6 Mott–Schottky plots collected at a frequency of 1 kHz in the dark for M-TiO$_2$ and HM-TiO$_2$ samples.

5 Subsequently, the effect of hydrogenation on the electronic properties of TiO$_2$ was investigated by Mott-Schottky plots (Fig. 6). Both HM-TiO$_2$ and M-TiO$_2$ exhibit positive slopes, as expected for n-type semiconductor. Additionally, the slope of HM-TiO$_2$ is relatively smaller than that of M-TiO$_2$, conforming
10 enhanced donor densities (carrier densities) after hydrogenation according to the following Mott-Schottky equation:

$$N_d = (2/e_0 \varepsilon \varepsilon_0) \left[d(1/C^2)/dV \right]^{-1}$$

It should be noted that this Mott-Schottky equation was derived based on the planar structure. Nevertheless, a qualitative
15 comparison of carrier densities between HM-TiO$_2$ and M-TiO$_2$ was reasonable because of their similar nanostructure. The increased donor density is due to the introduction of Ov, which functions as shallow electron donor, thus improving the electrical conductivties of TiO$_2$ and enhancing the separation efficiency of
20 the photogenerated electron-hole pairs.[11]
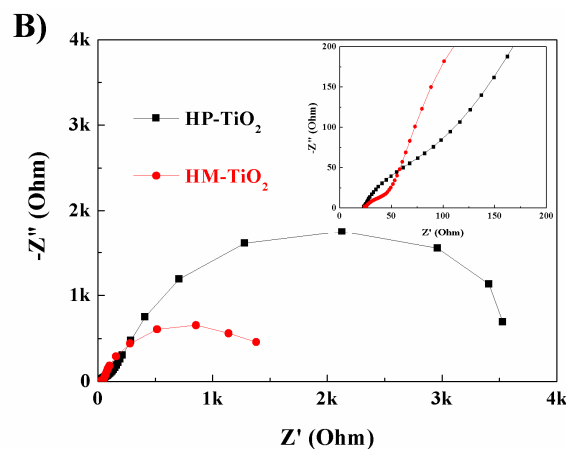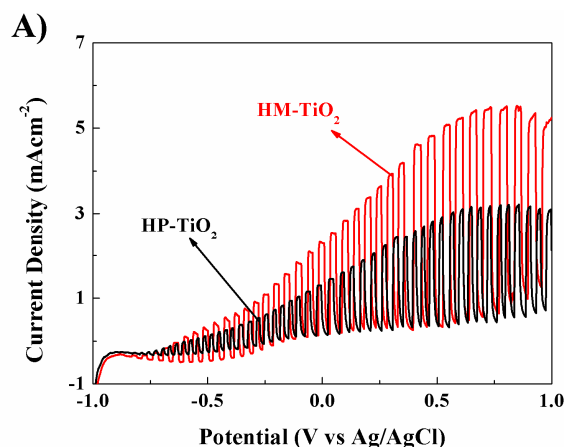
Fig. 7 (A) Chopped J-V curves collected from HM-TiO$_2$ and HP-TiO$_2$ at a
25 scan rate of 10 mV s-1 between -1.0 V and +1.0 V vs Ag/AgCl; (B) EIS of HM-TiO$_2$ and HP-TiO$_2$ in Nyquist plots in 0.5 M NaSO$_4$ under simulated solar illumination at a dc potential of 0 V vs Ag/AgCl with an ac potential of 5 mV between frequency range from 100 kHz to 100 mHz. The inset is the expanded range of ordinate and abscissa in the high frequency region.
30 The dots with different symbols are the measured data, while, the solid lines are the fitted results.

In order to study the promotion mechanism of the separation efficiency of photogenerated electrons-holes, the chopped *J-V* curves and EIS of HP-TiO$_2$ and HM-TiO$_2$ were measured in this
35 work and the results were shown in Figure 7. For both of HP-TiO$_2$ and HM-TiO$_2$, the photocurrent densities increase gradually with the applied potential before leveling off to a steady photocurrent (Fig. 7A). Furthermore, the photocurrent density of the HM-TiO$_2$ sample is substantially higher than that of the HP-
40 TiO$_2$ sample in the whole range of potentials studied. The maximum photocurrent density of HP-TiO$_2$ sample is approxiamtely 2.8 mAcm^{-2}, while that of the HM-TiO$_2$ sample is approxiamtely 5.2 mAcm^{-2}. The photocurrents of the HM-TiO$_2$ are almost 2-fold higher than that of the HP-TiO$_2$, confirming that
45 the nanoarchitecture is playing a positive role on the photoelectrochemical performance. In addition, the onset potential for the HM-TiO$_2$ sample negatively shifts to -0.83 V *vs* Ag/AgCl, compared with -0.78 V *vs* Ag/AgCl for the HP-TiO$_2$ sample. The negative shift of onset potential indicates that the
50 charge separation and transportation in the HM-TiO$_2$ are more efficient, achieving an enhanced photocurrent.

EIS was employed to obtain a deeper insight into the interface electron-transfer kinetics occurring at HM-TiO$_2$ samples. Figure 7B shows the EIS responses of HM-TiO$_2$ and HP-TiO$_2$ films
55 under illumination and the equivalent circuit is shown in Fig. S3 (ESI†). For this system, the Nyquist plots represent two semicircles in the frequency range between 100 mHz and 100 kHz. The semicircle in high frequency regions is assigned to the electron transport between the particles, and the one in the low
60 frequency region corresponds to the charge transfer at the electrode/electrolyte interface.[38] As shown in the inset of Fig. 7B, the semicircle or electron-transfer resistance of HP-TiO$_2$ is too large because electrons have difficulty to pass through the particle boundaries. For HM-TiO$_2$, the semicircle or electron-
65 transfer resistance decreases obviously, suggesting that the HM-TiO$_2$ serves as efficient transport paths for photogenerated

electrons. The most remarkable in the EIS results is the drastic change in the low frequency region. In contrast with the large semicircle diameter of HP-TiO₂, an extremely small semicircle diameter for HM-TiO₂ was observed, indicating that the reactions by electron transfer at the electrode/electrolyte interface should be further facilitated.[38,39] It means that the hierarchical nanostructure is beneficial for the charge separation, due to the augment in the active surface and an electronic conducting framework. The results of EIS are in good agreement with the above linear sweep voltammograms. These results confirmed that the construction of hierarchical nanostructure is conducive to accelerate the electron transfer process.

Conclusion

In conclusion, the hydrogenated TiO_2 mesoporous spheres with hierarchical structure consisting of primary nanoparticles with ∼ 15 nm in diameter and secondary colloidal spheres with 500-550 nm in diameter, have been prepared via a facile template-free strategy and subsequently hydrogen treatment. The obtained HM-TiO₂ exhibits an enhanced photocatalytic performance, which might be predominantly attributed to the introduction of hierarchical mesoporous structure besides Ov. Firstly, Ov not only boosts the light absorption but also improves the electrical conductivities of TiO_2, thus enhancing the optical response and electron-hole separation. Secondly, the HM-TiO₂ possesses large surface/volume ratio increases the electrode/electrolyte contact areas and catalytic active sites. More importantly, high accessible porosity and few grain boundaries provide a short path distance for electronic and ionic transport or mass transport, which improve the electron transport efficiency. In addition, the large microscale particles can allow multiple reflections of UV light, which enhances the photon absorption and thus increases the amount of photogenerated electrons and holes available to participate in the photocatalytic process. To some extent, these results may provide a new strategy to design some photocatalysts for the environmental cleaning and energy harvest.

Acknowledgements

Notes and references

Key Laboratory of Marine Environmental Corrosion and Bio-fouling, Institute of Oceanology, Chinese Academy of Sciences, 7 Nanhai Road, Qingdao 266071, China; Fax: +86-532-82880498; Tel: +86-532-82898731;

Corresponding author, Prof. Zhuoyuan Chen;
Email: zychen@qdio.ac.cn;
† Electronic Supplementary Information (ESI) available: [details of SEM and HRTEM of HP-TiO₂; XPS survey spectra and Overlay of normalized Ti 2p XPS spectra of M-TiO₂ and HM-TiO₂ and Equivalent circuit modelvfor EIS should be included here]. See DOI: 10.1039/b000000x/

1. A. Fujishima and K. Honda, *Nature*, 1972, **238**, 37-38.
2. F. Lei, Y. Sun, K. Liu, S. Gao, L. Liang, B. Pan and Y. Xie, *J. Am. Chem. Soc.*, 2014, **136**, 6826-6829.
3. G. M. Wang, Y. C. Ling, H. Y. Wang, X. Y. Yang, C. C. Wang, J. Z. Zhang and Y. Li, *Energy Environ. Sci.*, 2012, **5**, 6180-6187.
4. S. S. Zhang, S. Q. Zhang, B. Y. Peng, H. J. Wang, H. Yu, H. H. Wang and F. Peng, *Electrochem. Commun.*, 2014, **40**, 24-27.
5. Z. Lin, A. Orlov, R. M. Lambert and M. C. Payne, *J. Phys. Chem. B*, 2005, **109**, 20948-20952.
6. Z. K. Zhang, M. L. Bai, D. Z. Guo, S. M. Hou and G. M. Zhang, *Chem. Commun.*, 2011, **47**, 8439-8441.
7. C. H. Chen, J. Shieh, S. M. Hsieh, C. L. Kuo and H. Y. Liao, *Acta Mater.*, 2012, **60**, 6429-6439.
8. D. C. Cronemeyer, *Phys. Rev.*, 1959, **113**, 1222-1226.
9. A. Naldoni, M. Allieta, S. Santangelo, M. Marelli, F. Fabbri, S. Cappelli, C. L. Bianchi, R. Psaro and V. Dal Santo, *J. Am. Chem. Soc.*, 2012, **134**, 7600-7603.
10. A. Janotti, J. B. Varley, P. Rinke, N. Umezawa, G. Kresse and C. G. Van de Walle, *Phys. Rev. B*, 2010, **81**, 085212.
11. G. Wang, H. Wang, Y. Ling, Y. Tang, X. Yang, R. C. Fitzmorris, C. Wang, J. Z. Zhang and Y. Li, *Nano Lett.*, 2011, **11**, 3026-3033.
12. X. D. Jiang, Y. P. Zhang, J. Jiang, Y. S. Rong, Y. C. Wang, Y. C. Wu and C. X. Pan, *J. Phys. Chem. C*, 2012, **116**, 22619-22624.
13. H. Wang, G. Wang, Y. Ling, M. Lepert, C. Wang, J. Z. Zhang and Y. Li, *Nanoscale*, 2012, **4**, 1463-1466.
14. F. M. Pesci, G. Wang, D. R. Klug, Y. Li and A. J. Cowan, *J. Phys. Chem. C*, 2013, **117**, 25837-25844.
15. S. Li, J. Qiu, M. Ling, F. Peng, B. Wood and S. Zhang, *ACS Appl. Mater. Interfaces*, 2013, **5**, 11129-11135.
16. A. T. Bell, *Science*, 2003, **299**, 1688-1691.
17. E. Hendry, M. Koeberg, B. O'Regan and M. Bonn, *Nano Lett.*, 2006, **6**, 755-759.
18. E. Yagi, R. R. Hasiguti and M. Aono, *Phys. Rev. B: Condens. Matter*, 1996, **54**, 7945-7956.
19. Y. Li and J. Z. Zhang, *Laser Photonics Rev.*, 2010, **4**, 517-528.
20. K. Sivula, F. Le Formal and M. Gratzel, *ChemSusChem*, 2011, **4**, 432-449.
21. S. S. Zhang, S. Q. Zhang, B. Y. Peng, H. J. Wang, H. Yu, H. H. Wang and F. Peng, *Electrochem. Commun.*, 2014, **40**, 24-27.
22. D. A. Wheeler, Y. Ling, R. J. Dillon, R. C. Fitzmorris, C. G. Dudzik, L. Zavodivker, T. Rajh, N. M. Dimitrijevic, G. Millhauser, C. Bardeen, Y. Li and J. Z. Zhang, *J. Phys. Chem. C*, 2013, **117**, 26821-26830.
23. J. Ferber and J. Luther, *Sol. Energy Mater. Sol. Cells*, 1998, **54**, 265-275.
24. Q. F. Zhang, T. P. Chou, B. Russo, S. A. Jenekhe and G. Cao, *Adv. Funct. Mater.*, 2008, **18**, 1654-1660.
25. S. Nishimura, N. Abrams, B. A. Lewis, L. I. Halaoui, T. E. Mallouk, K. D. Benkstein, J. van de Lagemaat and A. J. Frank, *J. Am. Chem. Soc.*, 2003, **125**, 6306-6310.
26. D. R. Rolison, *Science*, 2003, **299**, 1698-1701.
27. W. Zhou, W. Li, J. Q. Wang, Y. Qu, Y. Yang, Y. Xie, K. Zhang, L. Wang, H. Fu and D. Zhao, *J. Am. Chem. Soc.*, 2014, **136**, 9280-9283.
28. C. Y. Yan, W. T. Yi, H. M. Yuan, X. X. Wu and F. Q. Li, *Environ. Prog. Sustainable Energy*, 2014, **33**, 419-429.
29. L. Shi, L. Liang, J. Ma, F. Wang and J. Sun, *Dalton Trans.*, 2014, **43**, 7236-7244.
30. X. Y. Zhang, X. Chen, S. M. Dong, Z. H. Liu, X. H. Zhou, J. H. Yao, S. P. Pang, H. X. Xu, Z. Y. Zhang, L. F. Li and G. L. Cui, *J. Mater. Chem.*, 2012, **22**, 6067-6071.
31. B. Oregan, J. Moser, M. Anderson and M. Gratzel, *J. Phys. Chem.*, 1990, **94**, 8720-8726.
32. H. Q. Lu, B. B. Zhao, R. L. Pan, J. F. Yao, J. H. Qiu, L. Luo and Y. C. Liu, *RSC Adv.*, 2014, **4**, 1128-1132.
33. X. Chen, L. Liu, P. Y. Yu and S. S. Mao, *Science*, 2011, **331**, 746-750.
34. K. S. W. Sing, D. H. Everett, R. A. W. Haul, L. Moscou, R. A. Pierotti, J. Rouquerol and T. Siemieniewska, *Pure Appl. Chem.*, 1985, **57**, 603-619.

35. Z. Zheng, B. Huang, J. Lu, Z. Wang, X. Qin, X. Zhang, Y. Dai and M. H. Whangbo, *Chem. Commun.*, 2012, **48**, 5733-5735.
36. S. Hoang, S. P. Berglund, N. T. Hahn, A. J. Bard and C. B. Mullins, *J. Am. Chem. Soc.*, 2012, **134**, 3659-3662.
5 37. X. Lai, J. E. Halpert and D. Wang, *Energy Environ. Sci.*, 2012, **5**, 5604.
38. E. S. Kim, N. Nishimura, G. Magesh, J. Y. Kim, J. W. Jang, H. Jun, J. Kubota, K. Domen and J. S. Lee, *J. Am. Chem. Soc.*, 2013, **135**, 5375-5383.
10 39. W. H. Leng, Z. Zhang, J. Q. Zhang and C. N. Cao, *J. Phys. Chem. B*, 2005, **109**, 15008-15023.
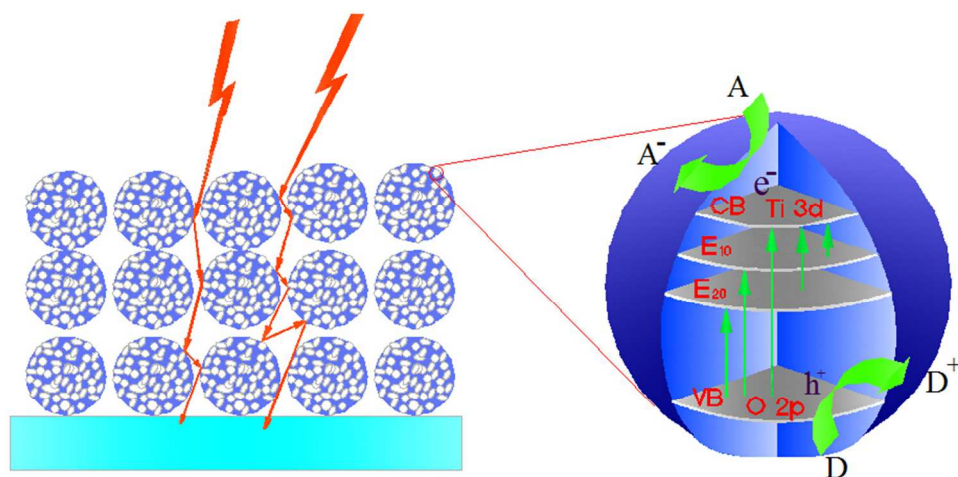
The hydrogenated TiO2 mesoporous spheres with hierarchical structure consisting of primary nanoparticles with ~ 15 nm in diameter and secondary colloidal spheres with 500-550 nm in diameter, have been prepared via a facile template-free strategy and subsequently hydrogen treatment.
253x123mm (96 x 96 DPI)